Multibranch Elastic Bound States in the Continuum

Shuowei An[1,*], Tuo Liu[2,3,*], Liyun Cao[4,*], Zhongming Gu,[5] Haiyan Fan[1], Yi Zeng[4]
Li Cheng[1,†], Jie Zhu,[5,‡] and Badreddine Assouar[4,§]

[1]*Department of Mechanical Engineering, Hong Kong Polytechnic University, Hong Kong, China*
[2]*Key Laboratory of Noise and Vibration Research, Institute of Acoustics, Chinese Academy of Sciences, Beijing 100190, China*
[3]*State Key Laboratory of Acoustics, Institute of Acoustics, Chinese Academy of Sciences, Beijing 100190, China*
[4]*Université de Lorraine, CNRS, Institut Jean Lamour, Nancy 54000, France*
[5]*Institute of Acoustics, School of Physics Science and Engineering, Tongji University, Shanghai 200092, China*

Constructing a highly localized wave field by means of bound states in the continuum (BICs) promotes enhanced wave-matter interaction and offers approaches to high-sensitivity devices. Elastic waves can carry complex polarizations and thus differ from electromagnetic waves and other scalar mechanical waves in the formation of BICs, which is yet to be fully explored and exploited. Here, we report the investigation of local resonance modes supported by a Lamb waveguide side-branched with two pairs of resonant pillars and show the emergence of two groups of elastic BICs with different polarizations or symmetries. Particularly, the two groups of BICs exhibit distinct responses to external perturbations, based on which a label-free sensing scheme with enhanced-sensitivity is proposed. Our study reveals the rich properties of BICs arising from the complex wave dynamics in elastic media and demonstrates their unique functionality for sensing and detection.

Introduction.—Enhancing wave-matter interaction through localized modes [1–3] is essential for achieving improved sensitivity [4–10], nonlinearity [11–13], and emission rate [14], which lays the foundation of many applications requiring high quality (Q) factors including lasers [15–17], biosensors [18,19], vortex generators [20–22], and other compact devices [23–26]. The localization of waves can be achieved in various ways such as topological states [1,2,27,28], in-gap defect modes [29,30], Anderson localization [31,32], nonlinearity [33–35], and the acoustic black hole effect [36–38], etc. An alternative way for energy "trapping" or "isolation," referred to as bound state in the continuum (BIC), rests on the mismatch between a localized state and all nearby extended states, which features complete suppression of radiation in an open environment. BICs have been realized in a wide variety of platforms such as photonic crystal slabs [39–41], coupled cavities [14,42], and waveguides [14,43–48].

BICs in elastic wave systems distinguish themselves from the acoustic and optic analogies by their intrinsic multiple polarizations, which suggest new physics and opportunities not available in other wave systems [49–51]. For example, a recent work utilized the polarization asymmetry between a solid resonator and its radiation channels (nonviscous fluid) to achieve genuine elastic BICs, going beyond the so-called "nonexistence theorem" for BIC construction [52]. Maznev and Every [51] showed the uniqueness of elastic wave systems in terms of

supporting non-symmetry-protected BIC without periodicity required in optical cases. In this Letter, by investigating the local modes of a Lamb waveguide side-branched with two pairs of resonant pillars, we reveal the polarizations not only play a key role in forming elastic BICs in different branches, but also enable these BICs to have distinct responses to various perturbations.

Theoretical analysis.—We consider the elastic wave propagation along a layer side branched with two pairs of pillars, which forms a pillared elastic waveguide [Fig. 1(a)]. The four identical pillars, acting as four resonators, are coupled via the waveguide hosting Lamb wave modes. d, t_s, t_p, and h_p are the spacing between the two columns of pillars, the waveguide thickness, and the thickness and height of the pillars, respectively ($t_s = 1$, $t_p = 1$, and $h_p = 16$ mm throughout this Letter). The reflection symmetry of the
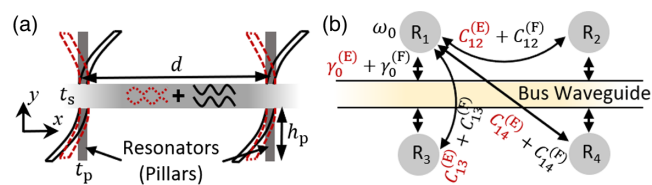

FIG. 1. Lamb waveguide with two pairs of side-branched resonators. (a) Schematic of the pillared elastic waveguide. It supports both extensional (red dashed line) and flexural waves (black solid line). (b) Model representation of the four resonators (R_1, R_2, R_3 and R_4) coupled via the bus waveguide. For simplicity, only the couplings of R_1 with other pillars are plotted.

pillars about the x axis guarantees the existence of two branches of decoupled local modes, namely, symmetric and antisymmetric modes [Fig. 1(a)]. For each branch of modes, the pillars are coupled exclusively via the zeroth-order Lamb waves with the same symmetry (viz. the extensional or flexural waves of a beam), which differs from the single-sided pillared waveguide with hybrid polarization [53]. The intrinsic losses caused by material damping and weak vibro-acoustic couplings are neglected if not specified.

We use coupled-mode theory (CMT) to describe the open elastic wave system [Fig. 1(b)]. The individual resonance behavior of the four identical pillars is characterized by $\omega' = \omega_0 + i\gamma_0$, in which ω_0 and γ_0 represent the resonance frequency and radiative decay rate, respectively. The coupling between two different pillars R_i and R_j is defined as C_{ij} with $i \neq j$ and $i, j = 1, 2, 3, 4$. The temporal coupled-mode equations are written as $i\partial A/\partial t = HA$ with $A = [A_1, A_2, A_3, A_4]^T$ representing the amplitude vector. Since the CMT simplifies the pillars as lumped resonators with a specific flexural mode, the vector can be quantified either by the horizontal displacements or rotations of the pillar ends. The non-Hermitian Hamiltonian, H, takes the form

$$H = \begin{pmatrix} \omega' & C_{12} & C_{13} & C_{14} \\ C_{21} & \omega' & C_{23} & C_{24} \\ C_{31} & C_{32} & \omega' & C_{34} \\ C_{41} & C_{42} & C_{43} & \omega' \end{pmatrix}. \quad (1)$$

All couplings are reciprocal, namely, $C_{ij} = C_{ji}$. The reflection symmetries of the system about the x and y axes further yield $C_{12} = C_{34}$, $C_{14} = C_{23}$, and $C_{13} = C_{24}$. Considering the Lamb modes supported by the waveguide, the radiation and coupling can be expressed as the sum of the extensional and flexural components, $\gamma_0 = \gamma_0^{(E)} + \gamma_0^{(F)}$ and $C_{ij} = C_{ij}^{(E)} + C_{ij}^{(F)}$, where the superscript "E" or "F" represents extensional or flexural waves. Moreover, the decoupled nature of the extensional and flexural modes implies that $\gamma_0^{(F)} = 0(\gamma_0^{(E)} = 0)$ and $C_{ij}^{(F)} = 0(C_{ij}^{(E)} = 0)$ for the symmetric (anti-symmetric) local modes. The four eigenvalues of H are obtained and classified into two branches according to their symmetries of eigenvectors about the x axis as given in Table I.

For the symmetric branch, each pair of pillars at the same site oscillates in-phase and radiates as a monopole [Fig. 1(a)]. These two monopoles are coupled solely with extensional wave. The far-field coupling between the resonators is expressed as the radiative decay rate multiplied by a propagation phase delay $C_{ij}^{(E)} = \gamma_0^{(E)} e^{-ik^{(E)}d}$, in which $k^{(E)}$ denotes the extensional wave number. The two eigenvalues of the symmetric (denoted by superscript "S") branch can thus be obtained as

TABLE I. Eigenvalues and eigenvectors of the Hamiltonian.

Branch	Eigenvalue	Eigenvector
Symmetric	$\omega_0 + (i\gamma_0^{(E)} + C_{13}^{(E)}) \pm (C_{12}^{(E)} + C_{14}^{(E)})$	$[\pm 1, 1, \pm 1, 1]$
Antisymmetric	$\omega_0 + (i\gamma_0^{(F)} - C_{13}^{(F)}) \pm (C_{12}^{(F)} - C_{14}^{(F)})$	$[\mp 1, -1, \pm 1, 1]$

$$\omega_\pm^{(S)} = \omega_0 + i2\gamma_0^{(E)}(1 \pm e^{-ik^{(E)}d}). \quad (2)$$

Remarkably, BIC occurs for vanishing imaginary part of $\omega_\pm^{(S)}$, which corresponds to the condition $k^{(E)}d = n\pi$, $(n \in \mathbf{Z})$. This is similar to the two-resonator acoustic system [3,44]. The BIC is a Friedrich-Wintgen (FW) BIC for $n = 0$ (i.e., d approaches zero) and a Fabry-Perot (FP) BIC [3] for $n \neq 0$.

The antisymmetric case is in stark contrast to the symmetric case as a result of the out-of-phase motion of the two pillars at the same site. Each pair of pillars radiate as a dipole and are coupled to the waveguide through flexural wave [Fig. 1(a)]. The far-field couplings between the two individual pillars are expressed as $-i\gamma_0^{(F)}e^{-i(k^{(F)}d - \pi/2)}$, which contains a $\pi/2$ initial phase in addition to the propagation phase delay $k^{(F)}d$. Additionally, considering the always out-of-phase oscillation of the pillars on different sides of waveguide for flexural-wave coupling, i.e., R_1 and R_3 as well as R_1 and R_4, an additional phase, $e^{i\pi}$, should be introduced when expressing their far-field couplings with radiative decay rate. Overall, the couplings are expressed as $C_{13}^{(F)} = i\gamma_0^{(F)}e^{i\pi}$, $C_{12}^{(F)} = i\gamma_0^{(F)}e^{-i(k^{(F)}d - \pi/2)}$, and $C_{14}^{(F)} = i\gamma_0^{(F)}e^{i\pi}e^{-i(k^{(F)}d - \pi/2)}$. The eigenvalues for the antisymmetric (denoted by superscript "A") case are

$$\omega_\pm^{(A)} = \omega_0 + i2\gamma_0^{(F)}[1 \pm e^{-i(k^{(F)}d - \frac{\pi}{2})}]. \quad (3)$$

Note that compared with the symmetric case [Eq. (2)], Eq. (3) has an additional $\pi/2$ phase difference. The forming condition of antisymmetric BICs is given by vanishing $\mathrm{Im}(\omega_\pm^{(A)})$ as $k^{(F)}d = n\pi + \pi/2$, $(n \in \mathbf{Z})$.

BICs and quasi-BICs in the pillared Lamb waveguide.—To test the above analysis, we conduct 2D simulations under plane strain assumption using both the eigenvalue and frequency domain solvers of the solid mechanics module, COMSOL Multiphysics (v5.6). Perfectly matched layers are applied to the two ends of the waveguide to mimic outgoing boundary conditions (BCs) [63]. The base material is aluminum with its density, Young's modulus, and Poisson ratio being 2700 kg/m^3, 76.27 GPa, and 0.32, respectively. As predicted by CMT, the simulated eigenfrequencies show there exist two branches of local resonant modes, the antisymmetric and symmetric branches denoted as A_e and S_e, $(e \in \mathbb{N})$, respectively, in which the subscript e
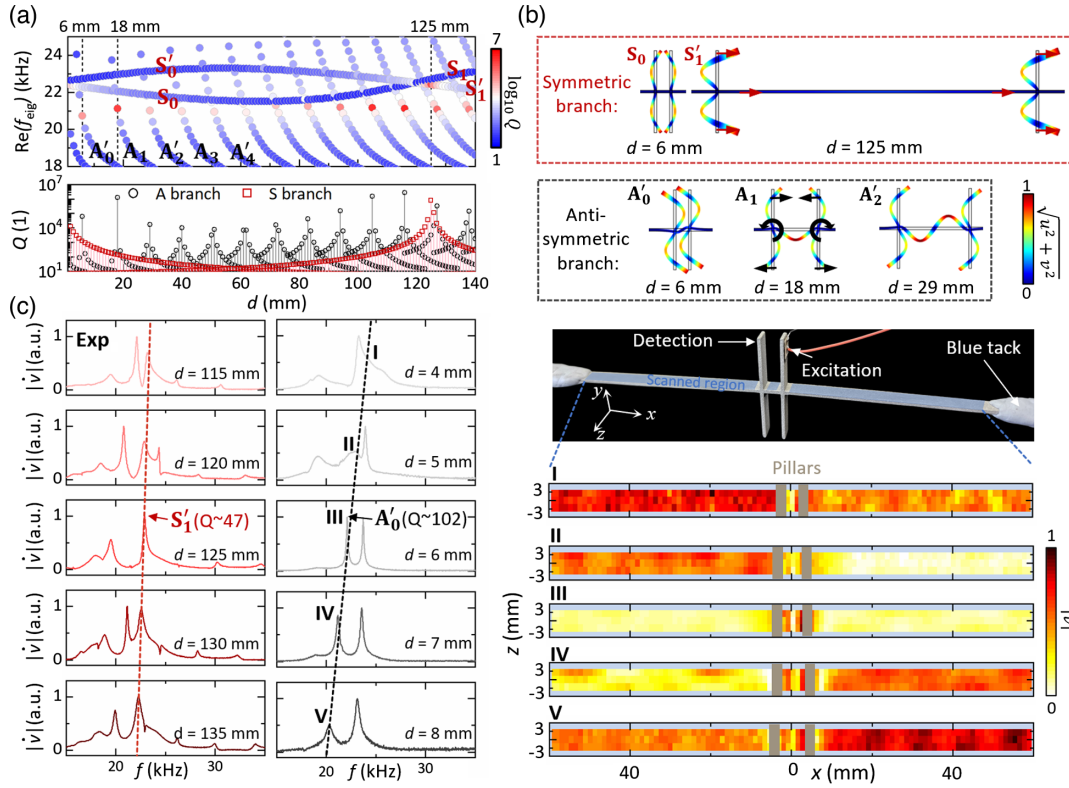
FIG. 2. BICs and quasi-BICs in pillared elastic waveguide. (a) Resonance frequencies [the real part of eigenfrequency, $\text{Re}(f_{\text{eig}})$] and Q factors of the antisymmetric and symmetric branches of eigenmodes as a function of d. The color scale represents the amplitude of Q in decibels (dB). (b) Mode shapes of the corresponding BICs and quasi-BICs. u and v are horizontal (x) and vertical (y) displacement components. (c) Measured frequency response and field distributions for the local modes in branch A_0' and S_1'. Left panel: frequency response functions (FRFs) of vertical velocity component $|\dot{v}|$. The dotted lines trace the peaks of S_1' and A_0'. Upper right panel: photo of the sample and experimental setup. Lower right panel: field distributions of $|\dot{v}|$ at the peaks I–V marked in the left panel (see animations of fields in [53]).

represents the vibrational order of the region between pillars and a prime is used to distinguish if the mode shape is antisymmetric or symmetric along the waveguide [Figs. 2(a) and 2(b)]. These modes display vanishing imaginary part $[Q = \text{Re}(\omega)/(2\text{Im}(\omega) \to \infty]$ for specific values of d, which are recognized as BICs [44]. A slight parameter detuning generally results in leaky modes with nonzero yet extremely small radiative loss, which are termed quasi-BICs [13,67,68].

For the symmetric branch, BICs appear when d is an integer multiple of the half wavelength (125 mm) [Fig. 2(b)]. These BICs are formed through extensional-wave coupling among the pillars and do not involve any flexural-wave coupling, similar to that in an acoustic two-resonator system [3,44]. Regarding the antisymmetric case, multiple local modes can be observed in Fig. 2(a) owing to the much shorter wavelength of flexural waves than extensional waves. Each of them can evolve into a BIC at a particular spacing, e.g., A_0' at $d = 6$, A_1 at $d = 18$, and A_2' at $d = 29$ mm [Fig. 2(b)], overall consistent with the condition of BICs derived by Eq. (3). The couplings between

the pillars and waveguides can strongly alter the resonance frequencies as d varies, which leads to the transition of antisymmetric local modes from those formed by the lower-order pillar mode to those formed by the higher-order pillar mode [53]. Apart from the above eigenmode analysis, the multibranch BICs can be characterized from a scattering point of view [53].

Based on the simulation results, we 3D-print two groups of Aluminum pillared waveguide samples and perform experimental measurements of their frequency responses using a Doppler laser-vibrometer [53] [upper right panel of Fig. 2(c)] to characterize the BICs by examining the evolution of Q factors with varied d (five samples for the symmetric branch S_1' with $d = 115, 120, 125, 130, 135$ mm; five samples for the anti-symmetric branch A_0' with $d = 4, 5, 6, 7, 8$ mm). The sample ends are covered with damping materials (blue tacks, ldj-01, bostik) to minimize boundary reflections. The excitation source is a piezo patch (PZT-5H) polarized along its thickness direction. All samples are designed to be 5-mm-wide in the z direction, which is the same as the size of the piezo patch to ensure the

consistency in excitations and avoid the appearance of higher-order guided modes [53].

As expected, the Q factors approach their maxima at critical spacings in both S_1' and A_0' branches, i.e., $Q = 47$ at $d = 125$ mm and $Q = 102$ at $d = 6$ mm, suggesting the vicinities of a symmetric and an antisymmetric BICs, respectively. The Q factors decrease as d deviates from the critical spacings, as reflected in the broader and lower spectral peaks for S_1' and A_0'. The peak even disappears when $d = 4$ mm. Moreover, the scanned field distributions of the vertical velocity component ($|\dot{v}|$) for A_0' around the spectral peaks [lower right panel of Fig. 2(c)] display trapped flexural wave field within two pairs of pillars when $d = 6$ mm and become leaky once d deviates from 6 mm, further confirming the existence of antisymmetric BIC in A_0'. The experimental results are overall consistent with the simulation results [53].

Sensitivity analysis to perturbations.—Dynamic-based approaches, which recognize material, structural, or environmental perturbation by examining the changes in mode parameters such as mode shift, splitting, and broadening, have been used in techniques ranging from optical microcavity sensing [16,69] to nondestructive testing [64–66]. Below, we reveal the unique spectral responses of the multibranch BICs to different types of perturbations. We focus on the parameter case of $d = 18$ mm where there are a BIC (21141 Hz) in A_1 and a quasi-BIC ($22055 + 82i$ Hz) in S_0. Four types of perturbation are considered [Fig. 3]. The environmental perturbation refers to the fluctuation of surrounding temperature or hydrostatic pressure.

Since the flexural wave is fully trapped within the in-between region, the BIC in A_1 is rather sensitive to the inner beam perturbation in terms of mode shift [Fig. 3(a)] induced by varied effective mode mass. Such fully trapped property in turn results in the immunity of this BIC to the perturbation in the outer regions [Fig. 3(b)]. The BIC no longer exists if the perturbation is exerted at the pillar due to the detuned resonance and broken symmetry [Fig. 3(c)].

The quasi-BIC in S_0, however, is almost immune to the perturbation in the entire waveguide [Figs. 3(a) and 3(b)], due to the much larger extensional wavelength than perturbation size and the extremely weak in-plane motion interacting with pillars [53]. Besides, we note that the perturbation exerted at pillars also leads to perceivable mode shifts, though not as obvious as the antisymmetric BIC [Fig. 3(c)].

The two states react in similar manners to the environmental perturbation as evidenced by the simultaneous mode shifts [Fig. 3(d)]. They are still a BIC and a quasi-BIC since the forming conditions can always be met for global parameter variations.

The ideal "radiation continuum" guaranteed by outgoing BCs, however, are inaccessible in practical sensing
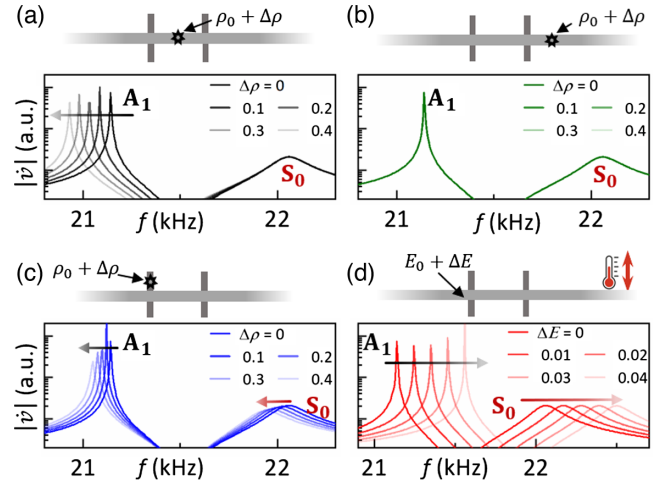

FIG. 3. Variations of the antisymmetric BIC in A_1 and symmetric quasi-BIC in S_0 branches against different types of perturbation: (a) in-between region, (b) outer region, (c) pillars, and (d) environment. In (a)–(c), the defect is mimicked by a $1 \text{ mm} \times 1 \text{ mm}$ inclusion with density being $\rho_0 + \Delta\rho$ and $\Delta\rho/\rho_0 \in \{0, 0.1, 0.2, 0.3, 0.4\}$ at particular locations. In (d) the environmental perturbation is introduced by varying the Young's modulus of the entire structure as $E_0 + \Delta E$ with $\Delta E/E_0 \in \{0, 0.01, 0.02, 0.03, 0.04\}$ [53].

application. Instead, we are commonly faced with finite structures. In this case, the BICs degenerate into the corresponding localized modes of a finite structure [53], which can no longer be termed BICs but inherit their properties. To demonstrate this, we replace the above outgoing BCs with fixed-free ends, in which the length of the beam is 160 mm. The BIC in A_1, quasi-BIC in S_0, and leaky mode in S_0', which exist in the infinite pillared waveguide [Fig. 2(a)], now respectively become modes A, S_I, and S_II of the finite beam.

In the simulated eigenfrequencies [Fig. 4(a)], mode A shows large frequency shift to the in-between defect as a result of strong wave-defect interaction of BIC, suggesting its high sensitivity. As a reference, mode C, the 14th flexural mode of the cantilever with the same dimensions but no pillars, is much less sensitive [Fig. 4(b)]. Modes S_I and S_II are immune to the defect yet shift in the same manner as mode A under the environmental perturbation, as the quasi-BIC in S_0 behaves.

The diverse sensitivities of the local modes are confirmed experimentally, as evidenced by the measured 651-Hz-shift of mode A, unshifted mode S_II and 89-Hz-shift of mode C in Fig. 4(c), in which the defect is mimicked by gluing an $1 \times 1 \times 10$ mm block on the sample [53]. The measured fields [Fig. 4(f)] further validate the properties of these local modes and their distinct responses to the defect, in stark contrast to modes C and C^d that appear as standing waves without any localization (see the comparison with simulation in [53]).
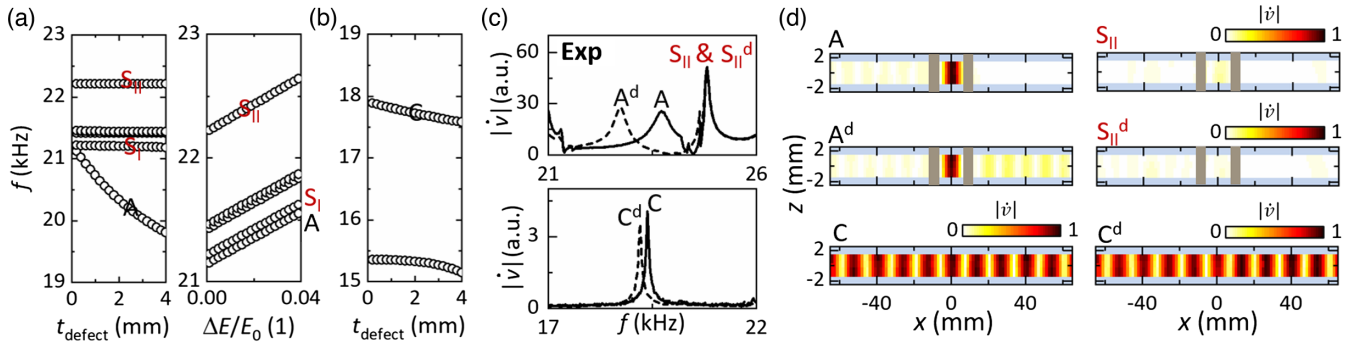
FIG. 4. Sensitivity analysis for local modes originated from multibranch BICs. (a) Simulated resonance frequencies of the local modes A, S_I and S_{II} as a function of the in-between defect strength (left panel) and environmental perturbation (right panel). The strengths of the defect and environmental perturbation are controlled by the thickness, t_{defect}, of an added block and the Young's modulus, $E_0 + \Delta E$, of the entire beam, respectively. (b) Simulated resonance frequencies of the bare beam as a function of defect strength. (c) Measured FRFs ($|\dot{v}|$) of the pillared (upper panel) and bare (lower panel) beams. The solid (dashed) lines represent the intact (defective) case. (d) Measured vertical velocity fields of modes A, A^d, S_{II}, S_{II}^d, C, and C^d.

Discussions.—The above unique responses of the local modes degenerated from the elastic multibranch BICs provide rich information about the local and global variations occurred in the waveguide, which may inspire novel schemes for detection or sensing. For example, based on the diverse sensitivities of mode A and mode S_{II} to the inner beam perturbation in combination with their uniform responses to environmental perturbation, the difference in their resonance frequencies can be defined as a new indicator to monitor material or structural change [53]. It enables us to easily eliminate unwanted environmental influences (temperature, prestress, etc.) from the overall mode shifts, contributing to a label-free high-performance sensing scheme to cope with varied working conditions.

Conclusions.—To conclude, we have theoretically and experimentally demonstrated the formation of BICs with different polarizations in a pillared Lamb waveguide. The symmetric configuration and multipolarized coupling lead to the decoupled symmetric and antisymmetric branches of local modes, which can evolve into BICs under certain conditions, depending on the monopolar or dipolar oscillation of the pairs of pillar resonators at the same site. These states display striking contrast in response to the in-between perturbation but vary similarly under environmental perturbation, which suggests a novel BIC-based sensing scheme. Our work reveals the rich polarization of BICs carried by elastic wave as well as their promising applications in areas of nondestructive testing and acoustic sensing.

*These authors contributed equally to this work.
†Corresponding author: li.cheng@polyu.edu.hk
‡Corresponding author: jiezhu@tongji.edu.cn
§Corresponding author: badreddine.assouar@univ-lorraine.fr.

[1] B. Xie, H.-X. Wang, X. Zhang, P. Zhan, J.-H. Jiang, M. Lu, and Y. Chen, Higher-order band topology, Nat. Rev. Phys. **3**, 520 (2021).

[2] H. Xue, Y. Yang, and B. Zhang, Topological acoustics, Nat. Rev. Mater. **7**, 974 (2022).

[3] C. W. Hsu, B. Zhen, A. Douglas Stone, J. D. Joannopoulos, and M. Soljačić, Bound states in the continuum, Nat. Rev. Mater. **1**, 16048 (2016).

[4] W. Xu, L. Xie, and Y. Ying, Mechanisms and applications of terahertz metamaterial sensing: A review, Nanoscale **9**, 13864 (2017).

[5] W. Suh, O. Solgaard, and S. Fan, Displacement sensing using evanescent tunneling between guided resonances in photonic crystal slabs, J. Appl. Phys. **98**, 033102 (2005).

[6] A. A. Yanik, A. E. Cetin, M. Huang, A. Artar, S. H. Mousavi, A. Khanikaev, John H. Connor, Gennady Shvets, and Hatice Altug, Seeing protein monolayers with naked eye through plasmonic Fano resonances, Proc. Natl. Acad. Sci. U.S.A. **108**, 11784 (2011).

[7] X. Fan and I. M. White, Optofluidic microsystems for chemical and biological analysis, Nat. Photonics **5**, 591 (2011).

[8] S. Romano, G. Zito, S. N. Lara Yépez, S. Cabrini, E. Penzo, G. Coppola, I. Rendina, and V. Mocellaark, Tuning the exponential sensitivity of a bound-state-in-continuum optical sensor, Opt. Express **27**, 18776 (2019).

[9] Y. Y. Chen, R. Zhu, M. V. Barnhart, and G. L. Huang, Enhanced flexural wave sensing by adaptive gradient-index metamaterials, Sci. Rep. **6**, 35048 (2016).

[10] Y. Chen, H. Liu, M. Reilly, H. Bae, and M. Yu, Enhanced acoustic sensing through wave compression and pressure

amplification in anisotropic metamaterials, Nat. Commun. **5,** 5247 (2014).

[11] F. Giorgianni *et al.*, Strong nonlinear terahertz response induced by Dirac surface states in Bi_2Se_3 topological insulator, Nat. Commun. **7,** 11421 (2016).

[12] E. N. Bulgakov and A. F. Sadreev, Robust bound state in the continuum in a nonlinear microcavity embedded in a photonic crystal waveguide, Opt. Lett. **39,** 5212 (2014).

[13] Z. Liu, Y. Xu, Y. Lin, J. Xiang, T. Feng, Q. Cao, J. Li, S. Lan, and J. Liu, High-Q quasibound states in the continuum for nonlinear metasurfaces, Phys. Rev. Lett. **123,** 253901 (2019).

[14] S. Huang *et al.*, Acoustic Purcell effect induced by quasi-bound state in the continuum, Fundamental Research **4**, 57 (2022).

[15] K. J. Vahala, Optical microcavities, Nature (London) **424,** 839 (2003).

[16] X. Jiang *et al.*, Whispering-gallery sensors, Matter Radiat. Extremes **3**, 371 (2020).

[17] Y. Zhi, X.-C. Yu, Q. Gong, L. Yang, and Y.-F. Xiao, Single nanoparticle detection using optical microcavities, Adv. Mater. **29,** 1604920 (2017).

[18] H. Altug, S.-H. Oh, S. A. Maier, and J. Homola, Advances and applications of nanophotonic biosensors, Nat. Nano-technol. **17,** 5 (2022).

[19] F. Yesilkoy, E. R. Arvelo, Y. Jahani, M. Liu, A. Tittl, V. Cevher, Y. Kivshar, and H. Altug, Ultrasensitive hyper-spectral imaging and biodetection enabled by dielectric metasurfaces, Nat. Photonics **13,** 390 (2019).

[20] A. Chen, W. Liu, Y. Zhang, B. Wang, X. Liu, L. Shi, L. Lu, and J. Zi, Observing vortex polarization singularities at optical band degeneracies, Phys. Rev. B **99,** 180101(R) (2019).

[21] Y. Guo, M. Xiao, and S. Fan, Topologically protected complete polarization conversion, Phys. Rev. Lett. **119,** 167401 (2017).

[22] H. M. Doeleman, F. Monticone, W. den Hollander, A. Alù, and A. F. Koenderink, Experimental observation of a polari-zation vortex at an optical bound state in the continuum, Nat. Photonics **12,** 397 (2018).

[23] Y. Wu, M. Yan, Z.-K. Lin, H.-X. Wang, F. Li, and J.-H. Jiang, On-chip higher-order topological micromechanical metamaterials, Sci. Bull. **66,** 1959 (2021).

[24] J. Cha, K. W. Kim, and C. Daraio, Experimental realization of on-chip topological nanoelectromechanical metamateri-als, Nature (London) **564,** 229 (2018).

[25] M. Yan, J. Lu, F. Li, W. Deng, X. Huang, J. Ma, and Z. Liu, On-chip valley topological materials for elastic wave manipulation, Nat. Mater. **17,** 993 (2018).

[26] J. Jin, X. Yin, L. Ni, M. Soljačić, B. Zhen, and C. Peng, Topologically enabled ultrahigh-Q guided resonances ro-bust to out-of-plane scattering, Nature (London) **574,** 501 (2019).

[27] M. Kim, Z. Jacob, and J. Rho, Recent advances in 2D, 3D and higher-order topological photonics, Light **9,** 130 (2020).

[28] H. Chen, H. Nassar, and G. L. Huang, A study of topo-logical effects in 1D and 2D mechanical lattices, J. Mech. Phys. Solids **117,** 22 (2018).

[29] O. Painter, R. K. Lee, A. Scherer, A. Yariv, J. D. O'Brien, P. D. Dapkus, and I. Kim, Two-dimensional photonic band-gap defect mode laser, Science **284,** 1819 (1999).

[30] S. Weimann, Y. Xu, R. Keil, A. E. Miroshnichenko, A. Tünnermann, S. Nolte, A. A. Sukhorukov, A. Szameit, and Y. S. Kivshar, Compact surface Fano states embedded in the continuum of waveguide arrays, Phys. Rev. Lett. **111,** 240403 (2013).

[31] L. Miglio, Introduction to the theory of disordered systems, Il Nuovo Cim. D **11,** 1375 (1989).

[32] P. Sheng, *Introduction to Wave Scattering, Localization and Mesoscopic Phenomena* (Springer, Berlin Heidelberg, 2006).

[33] D. K. Campbell, S. Flach, and Y. S. Kivshar, Localizing energy through nonlinearity and discreteness, Phys. Today **57,** No. 01, 43 (2004).

[34] Y. Lahini, A. Avidan, F. Pozzi, M. Sorel, R. Morandotti, D. N. Christodoulides, and Y. Silberberg, Anderson locali-zation and nonlinearity in one-dimensional disordered photonic lattices, Phys. Rev. Lett. **100,** 013906 (2008).

[35] M. Sato, B. E. Hubbard, and A. J. Sievers, Colloquium: Nonlinear energy localization and its manipulation in micromechanical oscillator arrays, Rev. Mod. Phys. **78,** 137 (2006).

[36] M. Mironov, Propagation of a flexural wave in a plate whose thickness decreases smoothly to zero in a finite interval, Sov. Phys. Acoust. **34**, 318 (1988).

[37] A. Pelat *et al.*, The acoustic black hole: A review of theory and applications, J. Sound Vibrat. **476,** 115316 (2020).

[38] L. Tang and L. Cheng, Loss of acoustic black hole effect in a structure of finite size, *Appl. Phys. Lett.* 109, 014102 (2016).

[39] B. Zhen, C. W. Hsu, L. Lu, A. Douglas Stone, and M. Soljačić, Topological nature of optical bound states in the continuum, Phys. Rev. Lett. **113,** 257401 (2014).

[40] A. G. Every, Guided elastic waves at a periodic array of thin coplanar cavities in a solid, Phys. Rev. B **78,** 174104 (2008).

[41] D. C. Marinica, A. G. Borisov, and S. V. Shabanov, Bound states in the continuum in photonics, Phys. Rev. Lett. **100,** 183902 (2008).

[42] S. Huang, T. Liu, Z. Zhou, X. Wang, J. Zhu, and Y. Li, Extreme sound confinement from quasibound states in the continuum, Phys. Rev. Appl. **14,** 021001(R) (2020).

[43] L. Huang, Y. K. Chiang, S. Huang, C. Shen, F. Deng, Y. Cheng, B. Jia, Y. Li, D. A. Powell, and A. E. Miroshnichenko, Sound trapping in an open resonator, Nat. Commun. **12,** 4819 (2021).

[44] L. Huang *et al.*, Topological supercavity resonances in the finite system, Adv. Sci. **9,** 2200257 (2022).

[45] *Introduction, in Ultrasonic Guided Waves in Solid Media*, edited by J. L. Rose (Cambridge University Press, Cam-bridge, England, 2014), pp. 1–15.

[46] K. F. Graff, in *Wave Motion in Elastic Solids*, edited by Karl F. Graff (Ohio State University Press, Columbus, 1975).

[47] L. Cao *et al.*, Perfect absorption of flexural waves induced by bound state in the continuum, Extreme Mech. Lett. **47,** 101364 (2021).

[48] L. Cao, Y. Zhu, Y. Xu, S.-W. Fan, Z. Yang, and B. Assouar, Elastic bound state in the continuum with perfect mode conversion, J. Mech. Phys. Solids **154,** 104502 (2021).

[49] A. Freedman, On resonance widths of leaky Lamb modes, J. Acoust. Soc. Am. **97**, 1980 (1995).

[50] E. Glushkov, N. Glushkova, and C. Zhang, Surface and pseudo-surface acoustic waves piezoelectrically excited in diamond-based structures, J. Appl. Phys. **112**, 064911 (2012).

[51] A. A. Maznev and A. G. Every, Bound acoustic modes in the radiation continuum in isotropic layered systems without periodic structures, Phys. Rev. B **97**, 014108 (2018).

[52] I. Deriy, I. Toftul, M. Petrov, and A. Bogdanov, Bound states in the continuum in compact acoustic resonators, Phys. Rev. Lett. **128**, 084301 (2022).

[53] See Supplemental Material at http://link.aps.org/supplemental/10.1103/PhysRevLett.132.187202, which incldues Refs. [3,42,44,48,54–66] for characterization of BICs from the scattering view of point, comparison between CMT and simulations, fumula for calibration-free detection, analysis of the Q factors of BICs, more practical implementation of the BICs-assisted probe, animations of fields, comparison between simulation and experimental results.

[54] A. Kodigala, T. Lepetit, Q. Gu, B. Bahari, Y. Fainman, and B. Kanté, Lasing action from photonic bound states in continuum, Nature (London) **541**, 196 (2017).

[55] S. Chintada, S. P. Dora, D. Kare, and S. R. Pujari, Powder metallurgy versus casting: Damping behavior of pure aluminum, J. Mater. Eng. Perform. **31**, 9122 (2022).

[56] W. Tan, Y. Sun, Z.-G. Wang, and H. Chen, Manipulating electromagnetic responses of metal wires at the deep subwavelength scale via both near- and far-field couplings, Appl. Phys. Lett. **104**, 091107 (2014).

[57] J. D. Achenbach, *Chapter 6—Withdrawn: Harmonic waves in waveguides, in Wave Propagation in Elastic Solids*, edited by J. D. Achenbach (Elsevier, Amsterdam, 1975), pp. 202–261.

[58] Y. Plotnik, O. Peleg, F. Dreisow, M. Heinrich, S. Nolte, A. Szameit, and M. Segev, Experimental observation of optical bound states in the continuum, Phys. Rev. Lett. **107**, 183901 (2011).

[59] H. Fan, B. Xia, L. Tong, S. Zheng, and D. Yu, Elastic higher-order topological insulator with topologically protected corner states, Phys. Rev. Lett. **122**, 204301 (2019).

[60] L. Cao, S. Wan, Y. Zeng, Y. Zhu, and B. Assouar, Observation of phononic skyrmions based on hybrid spin of elastic waves, Sci. Adv. **9**, eadf3652 (2023).

[61] Y. Liu, Z. Liang, J. Zhu, L. Xia, O. Mondain-Monval, T. Brunet, A. Alù, and J. Li, Willis metamaterial on a structured beam, Phys. Rev. X **9**, 011040 (2019).

[62] J. Zhu, Y. Liu, Z. Liang, T. Chen, and J. Li, Elastic waves in curved space: Mimicking a wormhole, Phys. Rev. Lett. **121**, 234301 (2018).

[63] L. Cao *et al.*, Pillared elastic metasurface with constructive interference for flexural wave manipulation, Mech. Syst. Sig. Process. **146**, 107035 (2021).

[64] M. I. N. Rosa, M. Mazzotti, and M. Ruzzene, Exceptional points and enhanced sensitivity in PT-symmetric continuous elastic media, J. Mech. Phys. Solids **149**, 104325 (2021).

[65] E. P. Carden and P. Fanning, Vibration based condition monitoring: A review, Struct. Health Monitoring **3**, 355 (2004).

[66] Y.-S. Lee and M.-J. Chung, A study on crack detection using eigenfrequency test data, Comput. Struct. **77**, 327 (2000).

[67] A. Krasnok, D. Baranov, H. Li, M.-A. Miri, F. Monticone, and A. Alú, Anomalies in light scattering, Adv. Opt. Photonics **11**, 892 (2019).

[68] S. Joseph, S. Pandey, S. Sarkar, and J. Joseph, Bound states in the continuum in resonant nanostructures: An overview of engineered materials for tailored applications, Nanophotonics **10**, 4175 (2021).

[69] J. Zhu, S. K. Ozdemir, Y.-F. Xiao, L. Li, L. He, D.-R. Chen, and L. Yang, On-chip single nanoparticle detection and sizing by mode splitting in an ultrahigh-Q microresonator, Nat. Photonics **4**, 46 (2010).